NANO · MICRO small
www.small-journal.com

Layer-by-Layer Assembly of Graphene Oxide and Silver Nanowire Thin Films with Interdigitated Nanostructure in Dendrite Suppressions of Li-Metal Batteries

Sojeong Won, Arum Jung, Kyeong Yeon Lim, Jinhan Cho, Jeong Gon Son, Hee-Dae Lim, and Bongjun Yeom**

Reducing the thickness of the Li-metal anode is key to enhancing the energy density of batteries. However, poor initial lithium deposition on Cu current collectors can exacerbate the growth of lithium dendrites and limit performance. This study explores innovative strategies by fabricating graphene oxide (GO) and silver nanowire (AgNW) thin films onto Cu-foil using the layer-by-layer (LbL) assembly method. The homogeneous LbL thin films are prepared with the assistance of bifunctional cross-linkers, such as cysteamine, to strengthen the intermolecular interactions between the nano-building blocks. The GO/AgNW LbL thin films possess a highly interdigitated nanostructure that combines the synergistic advantages of the individual building components. The GO layers facilitate the distribution of Li-ionic flux through the films, which promotes the formation of stable solid electrolyte interphase layers. In addition, the AgNW layers provide electrical pathways and serve as nucleation sites for Li—Ag alloy reactions. These combined effects lead to a flat and stable initial Li-deposition, as well as dense and compact Li growth, without significant dendrite formation. The full cell tests show excellent cycle longevity, 430 cycles with an N/P ratio of 3.36 at 1 C and 250 cycles with an N/P ratio of 1.81 at 3 C.

1. Introduction

Lithium (Li)-metal has attracted significant attention as one of the most promising next-generation anode materials for Li-based batteries, owing to its high theoretical capacity (3860 mAh g^{-1}).[1–3] However, its low electrochemical potential (−3.04 V vs the standard hydrogen electrode) presents challenges, including dendrite growth and poor cycle stability. The undesirable growth of Li dendrites and severe volume expansion during the plating/stripping cycles degrade the electrochemical performance of batteries and pose significant safety risks. This has been a major barrier to the widespread adoption of Li-metal anodes.[4] To fully utilize Li-metal anodes in high-energy-density batteries, minimizing the amount of Li-metal used in full cells is crucial. In this context, the negative/positive electrode capacity ratio (N/P ratio) should be kept below 2.0.[5,6] However, Li thin-film deposition onto a copper (Cu) foil (the typical anode current collector) is challenging due to its lithiophobicity. The initial Li deposition on Cu foil requires a high nucleation overpotential, mainly because of the significant thermodynamic mismatch between Li and Cu.[7–9] In addition, Li thin-film anodes struggle to compensate for the loss of fresh Li when it is consumed by the repetitive formation of solid-electrolyte-interphase (SEI) layers caused by dendritic growth. This further deteriorates cycling stability and capacity, particularly under high C-rate conditions.[10–12]

S. Won, A. Jung, K. Y. Lim, H.-D. Lim, B. Yeom
Department of Chemical Engineering
Hanyang University
Seoul 04763, Republic of Korea
E-mail: hdlim@hanyang.ac.kr; byeom@hanyang.ac.kr

The ORCID identification number(s) for the author(s) of this article can be found under https://doi.org/10.1002/smll.202412784

DOI: 10.1002/smll.202412784

J. Cho
Department of Chemical and Biological Engineering
Korea University
Seoul 02841, Republic of Korea

J. Cho, J. G. Son
KU-KIST Graduate School of Converging Science and Technology
Korea University
Seoul 02841, Republic of Korea

J. Cho, J. G. Son
Soft Hybrid Materials Research Center
Korea Institute of Science and Technology (KIST)
Seoul 02792, Republic of Korea

H.-D. Lim, B. Yeom
Department of Battery Engineering
Hanyang University
Seoul 04763, Republic of Korea

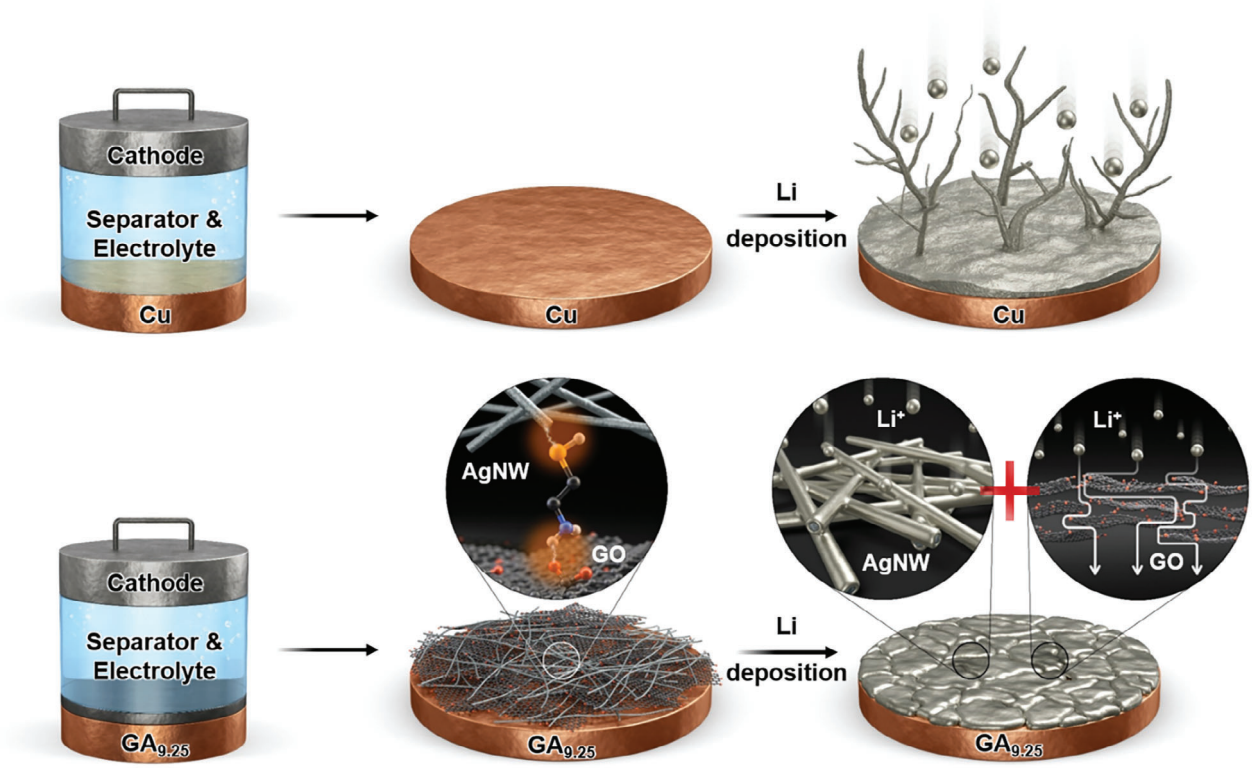

Figure 1. Schematic illustrating Li growth on bare Cu foil and the GO/AgNW LbL thin film-coated Cu foil. $GA_{9.25}$ refers to the $(GO/MEA/AgNW/MEA)_{9.25}$ LbL sample, which is the representative sample used in this study.

In order to address these problems, the surface of Cu foil can be modified using various approaches that make it possible to impart lithiophilic properties to the Cu current collectors. Typical examples include carbon-based materials,[13] metal materials such as Ag,[14] Au,[15] and Zn,[16] or mixtures of two or more materials.[17] For example, graphene oxide (GO) was utilized to distribute Li-ion flux and stable SEI formations.[18–20] Silver has been used frequently among metals, taking advantage of high electrical conductivity and high Li affinity by forming Li–Ag alloy with the solid solution interfaces.[21,22] More specifically, Ag nanowire (AgNW) coatings on the Cu foils were found to induce electrochemical alloying reactions by lowering the Li nucleation overpotentials.[23] Carbon and metal nanocomposites were combined for synergistic effects. Notable examples include GO-covered Zn metal nanoparticles[17] and Au-decorated carbon nanotube composites.[24] However, they still require many improvements to control lithiophilicity and address pulverization problems and low coulombic efficiency (CE).[25–27] In addition, many previous studies have demonstrated only limited performances under conditions of high N/P ratios (> 4) and low C-rates (< 1) (Table S1, Supporting Information).

Layer-by-layer (LbL) assembly methods have been used to prepare functional thin films with intermolecular interactions, such as electrostatic, hydrogen bonding, van der Waals, and other physical and chemical interactions.[28–32] These methods enabled various types of 0D, 1D, and 2D nanomaterials to be deposited onto the substrates in a controlled manner to impart specific functionalities for their purpose. Different coating methods can be used for the LbL assembly, including dip-coating, spin-coating, spray-coating, and roll-to-roll coating, all of which are suitable for large-scale production, as reported elsewhere.[33–35] In this study, we use LbL assembly methods to prepare GO and AgNW thin films with highly interdigitated nanostructures on Cu foils, which exhibit dendrite-suppression capabilities for Li-metal batteries (**Figure 1**). Moreover, GO and AgNW layers were alternatingly deposited onto the Cu foils via the LbL method. Cysteamine (MEA) layers were inserted between GO and AgNW layers to serve as bi-functional cross-linkers with short alkyl chains. The amine group at one end of MEA was bound to GO via covalent bonding, while the thiol group at the other end of MEA was linked to AgNW surfaces through coordinate bonding. These strong bindings at the interfaces help promote the stability and integrity of the interdigitated nanostructure. The LbL films enhanced Li-ion distribution, facilitated stable SEI layer formation,[17] and lowered nucleation energies, thanks to the synergistic advantages of the GO and AgNW components. This led to stable and flat Li deposition during the initial stage, while subsequent Li depositions formed compact and dense forms without dendritic growth. Symmetric cell tests with the GO and AgNW LbL thin film-coated Cu foils, pre-deposited with 4 mAh cm^{-2} of Li, demonstrated stable Li plating/stripping for over 400 cycles at 1 mA cm^{-2} and 1 mAh cm^{-2}. Full cell tests of the same samples with $LiFePO_4$ (LFP) cathodes exhibited significantly improved cycle stability, with 430 cycles at an N/P ratio of 3.36 at 1 C and 250 cycles at an N/P ratio of 1.81 at 3 C. This represents the longest cycle under similar harsh conditions compared to other studies using lithiophilically

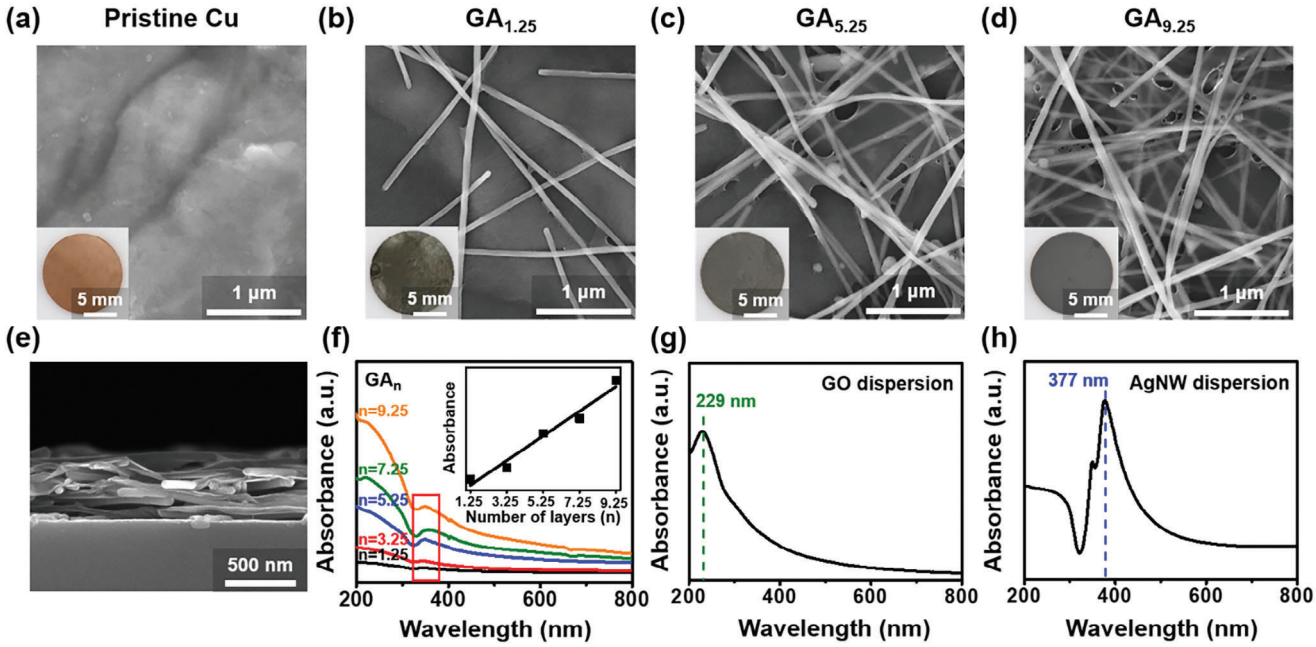

Figure 2. FE-SEM top-view images. a) Pristine Cu, b) $GA_{1.25}$, c) $GA_{5.25}$, and d) $GA_{9.25}$. The insets are photographs of the samples. e) FE-SEM cross-sectional image of $GA_{9.25}$. UV–vis absorbance spectra of f) GA_n, g) GO dispersion and h) AgNW dispersion. The inset in f) shows absorbances at 354 nm as the number of quadruple layers for GA_n increases.

modified Cu foil anodes—to the best of our knowledge (Table S1, Supporting Information). The LbL-assembly-based approach demonstrates great potential for fabricating high-energy-density Li-metal batteries with fast charging and discharging capabilities for future energy-storage devices.

2. Results and Discussion

2.1. LbL Assembly of GO/AgNW Thin Films with a Highly Interdigitated Nanostructure

GO/AgNW LbL thin films were prepared on Cu foil substrates via LbL assembly, which involved alternating deposits of GO and AgNW layers with intermediate cross-linker layers of MEA; for details, see the Experimental Section (Supporting Information). Briefly, the polyethyleneimine (PEI) pre-layer was deposited on the substrate to increase the adhesion of the following LbL depositions. GO was first deposited (using immersion) for 5 min, followed by washing off the weakly bound GOs. Then, the GO-deposited substrates were immersed in MEA solutions for 5 min to form GO/MEA layers on the substrates. Subsequently, AgNW and MEA layers were deposited on the substrates in the same manner to form the $(GO/MEA/AgNW/MEA)_{n=1}$ LbL layer on the substrates (Figure S1, Supporting Information). This will be referred to as the GA_1 sample, where n represents the number of repetitions of the quadruple layer set. For example, $GA_{9.25}$ indicates that the LbL process for the quadruple layers was repeated nine times, with the final GO layer deposited on top of the LbL-assembled films. All samples (including the GO layers) were prepared with a final coating of GO layers to promote the uniform distribution of Li ions on the electrode surface, leveraging the fast ion-diffusion properties of GO. This will be elaborated later (details are provided in the Experimental Section, Supporting Information). AgNWs synthesized by the polyol reduction method were used in the LbL depositions (details are provided in the Experimental Section, Supporting Information). The diameter and length of the synthesized AgNWs were 56 ± 13 nm and 9.8 ± 1.1 μm, respectively (Figure S2, Supporting Information). GO/AgNW LbL thin films were characterized through increased repetitions (n) (**Figure 2**). The field emission scanning electron microscopy (FE-SEM) images of Figure 2b–d reveal a gradual increase in surface coverage and randomly deposited amounts of GOs and AgNWs as n increased from 1.25 to 9.25. The photograph of the $GA_{1.25}$ sample in the inset of Figure 2b shows a dark gray color across the entire surface, a noticeable change from the Cu color of the pristine substrate (Figure 2a), indicating a uniform and homogeneous coating of the LbL components from the initial stage of assembly. Subsequent depositions displayed blackish and shiny colors, corresponding to the GO and AgNWs, respectively (insets of Figure 2b–d). The cross-sectional FE-SEM image of $GA_{9.25}$ shows a thickness of ≈400 nm with bonded instances of GO and AgNW layers (Figure 2e). In addition, the LbL assembly method is advantageous for preparing homogenous thin films with GO and AgNW. For example, simple casting of the mixture of the GO and AgNW dispersions typically leads to non-uniform coating due to their spontaneous aggregation and flocculation in the mixture (Figure S3a, Supporting Information).[36] In contrast, the bottom-up growth of the LbL assembly method, which relies on intermolecular interactions between the nano-building blocks, enabled smooth and homogeneous depositions for GA films with relatively large-sized samples (Figure S3b,c, Supporting Information).

UV–vis absorption measurements were performed on GA_n, AgNW dispersion, and GO dispersion to examine the deposition

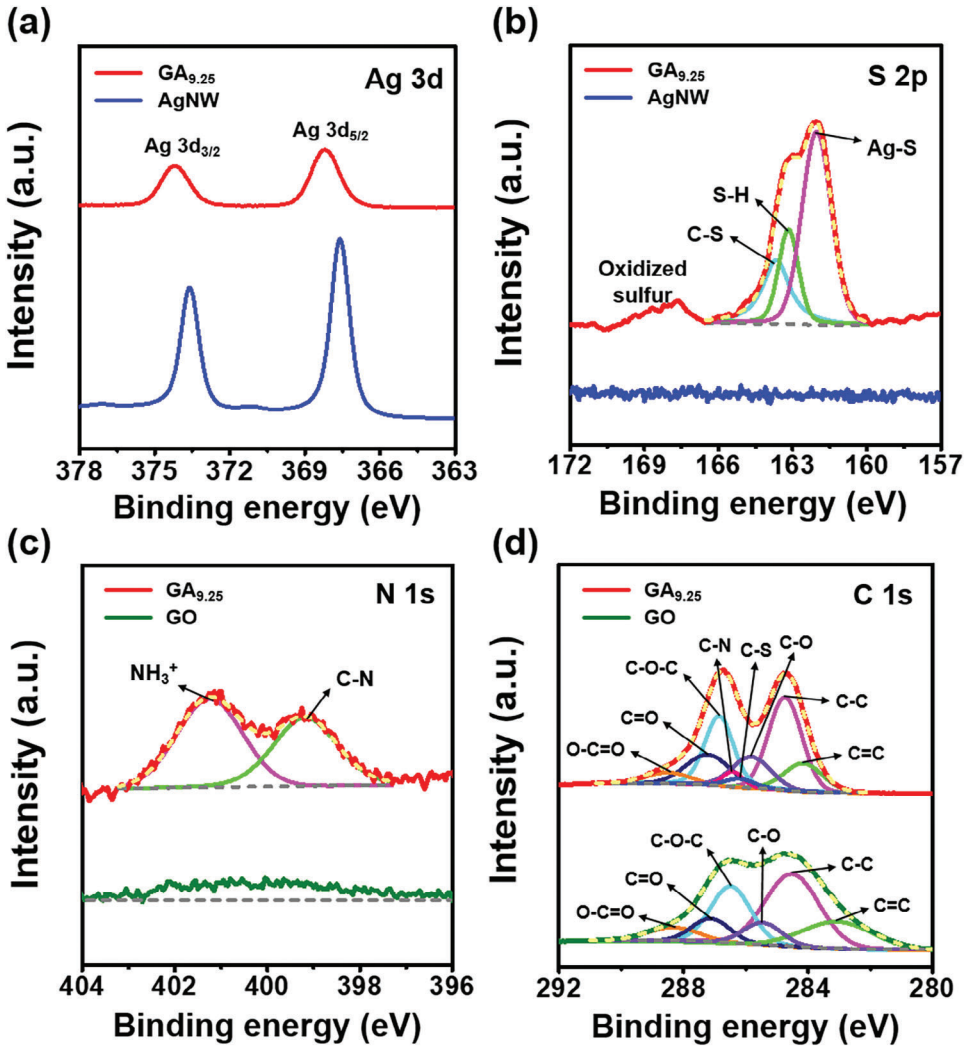

Figure 3. XPS spectra of a) Ag 3d and b) S 2p peaks for pristine AgNW and $GA_{9.25}$. c) N 1s and d) C 1s peaks for pristine GO and $GA_{9.25}$. The yellow dashed lines represent the summed spectra of the deconvoluted peaks.

behavior of LbL. The GA_n samples were measured after every two repetitions, with values of n = 1.25, 3.25, 5.25, 7.25, and 9.25. All GA_n samples exhibited two notable peaks at 220 and 354 nm, which are attributed to GO and AgNW, respectively (Figure 2f). The GO peaks attributed to the $\pi \rightarrow \pi^*$ transition were blue-shifted from the original peak position (229 nm) because of the reduced electronic conjugation and covalent bond (Figure 2g).[37,38] In addition, the AgNW peaks, attributed to the transverse mode of the surface plasmon of AgNWs, were also blue-shifted from the original peak (377 nm) due to coordination bonding and arrangement (Figure 2h).[39,40] The shoulder peaks at 300 nm in the GO dispersion, corresponding to the $n \rightarrow \pi^*$ transition, and at 349 nm in AgNW dispersion, attributed to the bulk silver plasmon, were difficult to discern in Figure 2f, possibly due to their weak intensities. The absorbance intensities of the GA_n samples gradually increased with the number of repetitions. The inset in Figure 2f shows a monotonic increase in the AgNW peak intensities for the GA_n samples, which indicates successful alternating depositions via the LbL assembly methods.

X-ray photoelectron spectroscopy (XPS) was performed to investigate the interaction between GO, AgNW, and MEA of the $GA_{9.25}$ (**Figure 3**). The Ag 3d peaks in $GA_{9.25}$ were at 368.2 and 374.2 eV for $3d_{5/2}$ and $3d_{3/2,}$ respectively. These shifted to higher binding energies than the same peaks for pristine AgNW at 367.6 and 373.6 eV, respectively (Figure 3a). Furthermore, $GA_{9.25}$ had a prominent S 2p peak near 162 eV and a minor peak at 167.6 eV from oxidized sulfur (Figure 3b). Note that the pristine AgNW did not show any S content. The prominent S 2p peak can be deconvoluted into three peaks at 162.0, 163.2, and 163.7 eV with relative peak areas of 55.6%, 19.4%, and 25.0%, respectively. The first deconvoluted peak can be attributed to the formation of coordination bonding between Ag and S via electron transfer after the LbL assembly between AgNW and MEA.[41] These results are consistent with the observed Ag 3d peak shifts. The remaining small peaks can be assigned to S—H and C—S bonds from the unreacted C—SH groups in MEA.[42] For the N 1s spectra, $GA_{9.25}$ depicts a merged peak from two deconvoluted peaks at 399.2 and 401.3 eV (Figure 3c). These can be attributed to C—N bonds from

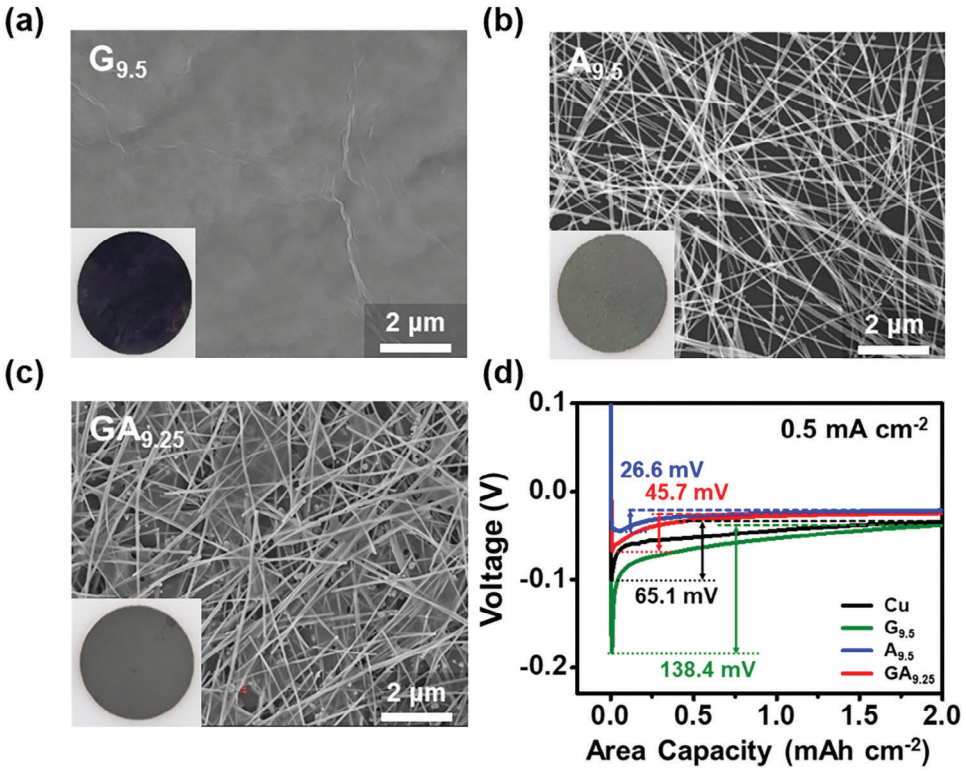

Figure 4. FE-SEM top-view images of a) $G_{9.5}$, b) $A_{9.5}$, and c) $GA_{9.25}$. The insets are optical photographs of each sample. d) Voltage-capacity profiles of Cu, $G_{9.5}$, $A_{9.5}$, and $GA_{9.25}$ in 1 M LiTFSI in DOL/DME (1:1) electrolyte with 1 wt% $LiNO_3$ additives at 0.5 mA cm^{-2}.

MEA and $-NH_3^+$ moieties from the protonated amino groups of MEA, respectively, which indicates MEA bonding to GO.[43] The pristine GO showed a slight hump in the same region that can be ignored. For the C 1s spectra, the pristine GO exhibited six deconvoluted peaks corresponding to C=C, C—C, C—O, C—O—C, C=O, and O—C=O (Figure 3d; Table S2, Supporting Information).[44] In the case of $GA_{9.25}$, additional peaks for C—N and C—S were observed with small peak areas due to binding with MEA cross-linkers,[45] which were not present in the pristine GO. In addition, for $GA_{9.25}$, the peak area ratio of C—O to C—O—C increased 1.6 times compared to the pristine GO (Table S2, Supporting Information). These changes can be attributed to ring-opening reactions of epoxide groups in GO caused by nucleophilic attack from the MEA amine groups.[46] To summarize the above results, it was confirmed that MEA, the bi-functional short cross-linker with thiol and amine groups at each end, was successfully bound to both the Ag and GO surfaces, respectively.

2.2. Li-Deposition Behavior of GO/AgNW LbL Film-Deposited Cu Foils for Li-Metal Anodes

To investigate the role of each LbL component and their combined effects in $GA_{9.25}$, the control samples comprised of only GO or AgNW were prepared separately on Cu foils. GO was paired with tris(2-aminoethyl)amine (TREN) to create the $(GO/TREN)_n$ LbL sample denoted as G_n. In addition, AgNWs were combined with ethane-1,2-dithiol (EDT) to obtain the $(AgNW/EDT)_n$ LbL sample denoted as A_n. For paired cross-linkers, short alkyl chain molecules with the same multifunctional moieties of either amines or thiols were selected for TREN or EDT, respectively. The number of repetitions for G_n or A_n was fixed at $n = 9.5$ to match the number of active layers in $GA_{9.25}$. FE-SEM images of $G_{9.5}$, $A_{9.5}$, and $GA_{9.25}$ are shown in **Figure** 4a–c. A smooth surface was obtained through homogeneous depositions of GO layers for the black $G_{9.5}$ sample in the inset photograph (Figure 4a). Random depositions of AgNWs were found for the $A_{9.5}$, which shows full coverage and appears dark gray in the inset of Figure 4b. $GA_{9.25}$ showed mixed depositions of GO and AgNW layers (Figure 4c). UV–vis absorption spectra of these samples during LbL assembly are shown in Figure S4 (Supporting Information). As the number of repetitions increased, the absorption of both G_n and A_n gradually increased, which indicates successful build-up for the LbL assembly.

Furthermore, the Li-deposition was investigated by observing the nucleation overpotentials for initial Li depositions and the morphologies after deposition in a half-cell set-up (Figure 4d; Figure S5, Supporting Information). Cu, $G_{9.5}$, $A_{9.5}$, and $GA_{9.25}$ were tested and compared using 1 M LiTFSI in DOL/DME (1:1) with 1 wt% $LiNO_3$ additives at current densities of 0.5 mA cm^{-2} and 1 mA cm^{-2} via voltage-capacity profiles. Cu and the only GO-coated Cu of $G_{9.5}$ exhibited the highest nucleation overpotentials of 65.1 and 138.4 mV, respectively. The high overpotential for Cu is due to lithiophobicity and is consistent with other values from the literature that were tested under similar conditions.[14,47] For $G_{9.5}$, this is possibly caused by its low electrical conductivity.[48] In contrast, $A_{9.5}$ and $GA_{9.25}$ displayed lower overpotential values of 26.6 and 45.7 mV, respectively. The same order was observed

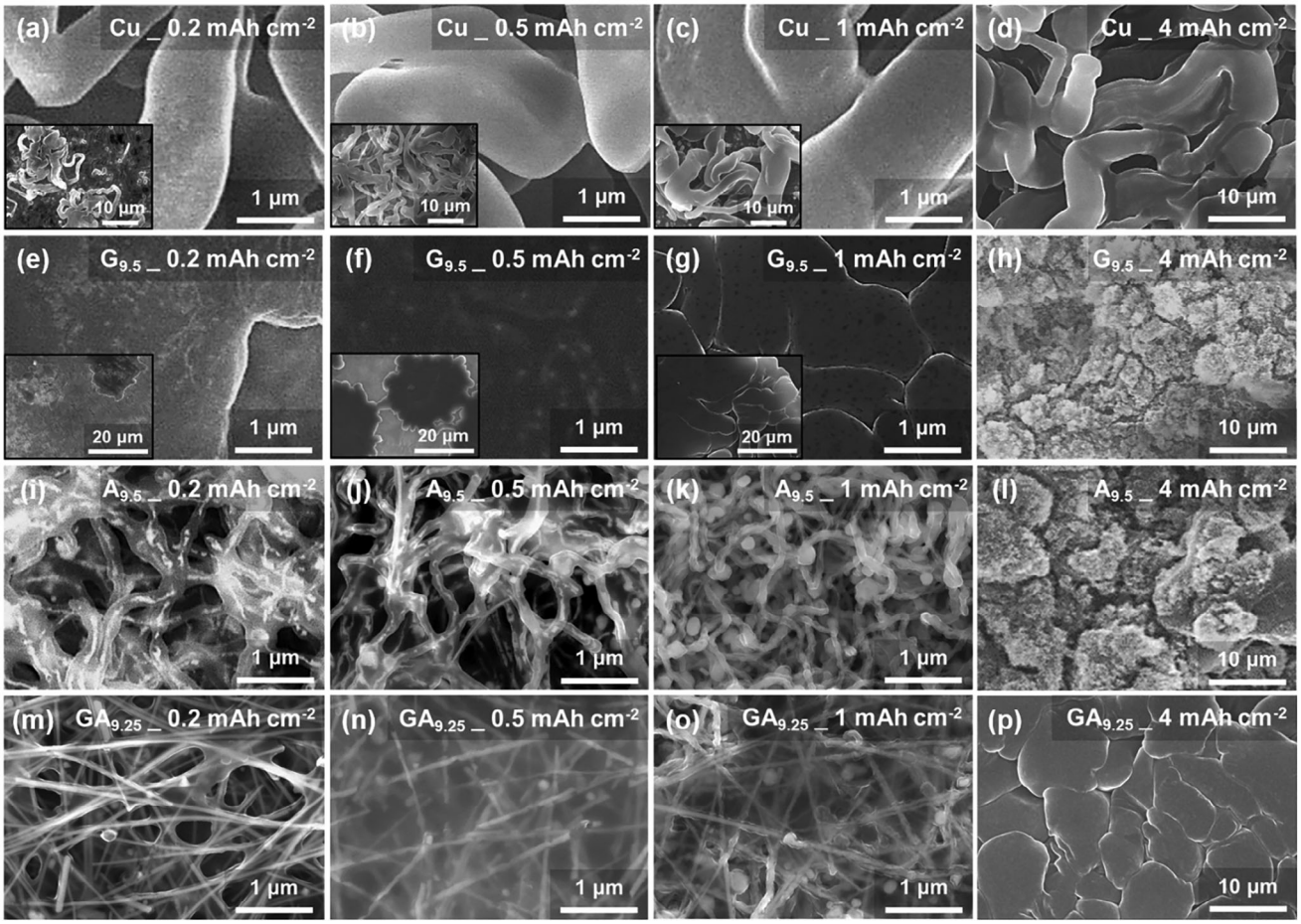

Figure 5. FE-SEM top-view images of a–d) Cu, e–h) $G_{9.5}$, i–l) $A_{9.5}$, and m–p) $GA_{9.25}$ after Li plating with different capacities at 0.5 mA cm^{-2}, (a,e,i,m) 0.2 mAh cm^{-2}, (b,f,j,n) 0.5 mAh cm^{-2}, (c,g,k,o) 1 mAh cm^{-2}, and (d,h,l,p) 4 mAh cm^{-2}. The insets are low-magnification images for the corresponding samples.

for a current density of 1 mA cm^{-2} (Figure S5, Supporting Information). This indicates that the AgNW layers in the LbL films exhibited a lower energy barrier for Li nucleation due to their lithiophilic characteristics. For $GA_{9.25}$, even with the alternating build-up of insulating GO layers, the sheet resistance was 2.16×10^{-1} Ohm sq^{-1}, which is six orders of magnitude lower in sheet resistance compared to $G_{9.5}$ with a sheet resistance of 1.55×10^{5} Ohm sq^{-1} (Table S3, Supporting Information). This can be attributed to the formation of a conductive network pathway with highly anisotropic AgNWs in the interdigitated nanostructures. As a result, $GA_{9.25}$ exhibited a low energy barrier for Li nucleation, which can synergize with the formation of a uniform and stable SEI, as explained in the following section.

FE-SEM analysis was performed to study the Li-deposition morphology for Cu, $G_{9.5}$, $A_{9.5}$, and $GA_{9.25}$ for different deposition amounts at a fixed current density of 0.5 mA cm^{-2} (**Figure 5**). For Cu, Li dendrites were already observed in specific areas, even with a very small amount of Li deposition (0.2 mAh cm^{-2}). Due to the poor affinity for Li, dendritic growth was observed locally, leaving other areas without significant Li deposits (insets of Figure 5a–c). As the Li deposition capacity increased to 2 and 4 mAh cm^{-2}, the dendrites grew significantly and covered the whole surface (Figure S6a, Supporting Information; Figure 5d). For $G_{9.5}$ (Figure 5e–g), the initial Li depositions show flat morphologies for 0.2, 0.5, and 1 mAh cm^{-2}, possibly due to in-plane ionic migration on the GO surfaces.[18] However, when Li deposition was increased to 2 and 4 mAh cm^{-2}, dendritic growth appeared across the flat Li surfaces, and a severe degree of dendritic formation can be observed over the entire area (Figure S6b, Supporting Information; Figure 5h). For $A_{9.5}$ (Figure 5i–j), Li–Ag alloy formation began on the AgNWs during the initial depositions of 0.2 and 0.5 mAh cm^{-2}. The pristine AgNW diameter of 57 nm increased to 185 nm due to the formation of the Li—Ag alloy. When Li was deposited at 1 mAh cm^{-2} (Figure 5k), Li began to deposit on top of the alloy nanowires. As the Li deposition increased to 2 and 4 mAh cm^{-2}, excess Li accumulated on the surfaces, forming uneven dendritic growths in much smaller sizes than those observed on Cu (Figure S6c, Supporting Information; Figure 5l).[41] In $GA_{9.25}$, initial Li deposition was uniform around the AgNWs at 0.2 mAh cm^{-2} (Figure 5m). As the capacity was further increased, Li–Ag alloy formations became more prominent, filling the inner spaces of the highly interdigitated nanostructure of $GA_{9.25}$ (Figure 5n–o). Notably, Figure 5n shows a flat and smooth surface attributed to stable SEI formations and

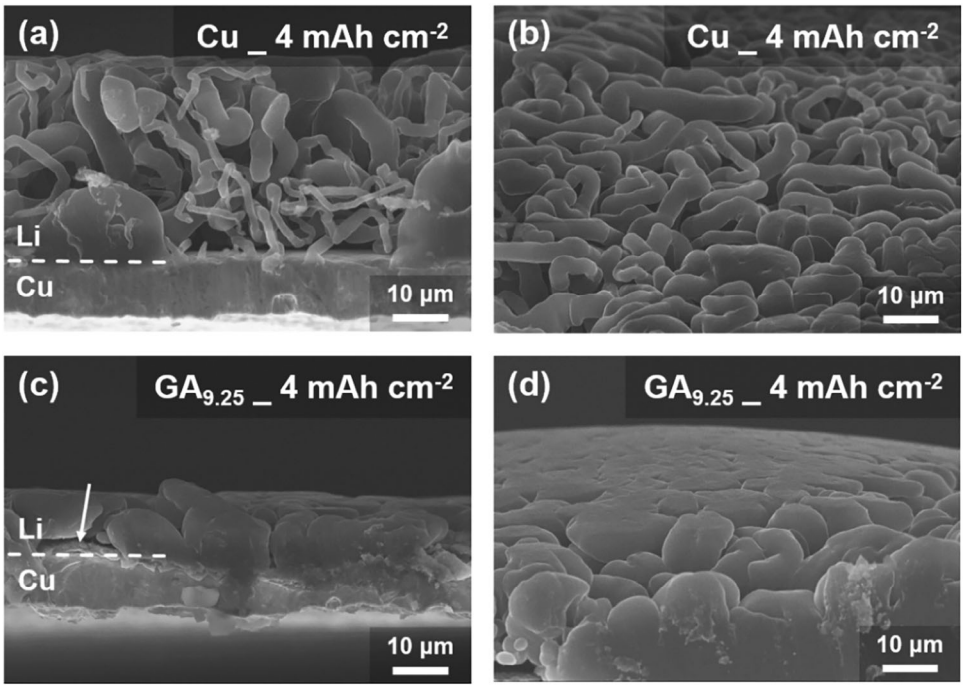

Figure 6. FE-SEM images of the Cu and $GA_{9.25}$ samples after Li plating at 0.5 mA cm^{-2} and 4 mAh cm^{-2}. a) Cu and c) $GA_{9.25}$ cross-section, and b) Cu and d) $GA_{9.25}$ at a tilt angle of 10°.

the even spreading of Li deposits throughout the interdigitated nanostructure facilitated by the GO layers. At higher Li depositions of 2 and 4 mAh cm^{-2}, Li grew uniformly in dense and compact forms without dendrite formation, in stark contrast to other control samples that exhibited dendritic morphologies (Figure S6d, Supporting Information; Figure 5p).

The Li-deposition morphologies of the cross-section and the 10°-tilted images of Cu and $GA_{9.25}$ were compared after Li deposition with a capacity of 4 mAh cm^{-2}. Cu shows Li dendrites growing from localized nucleation spots (**Figure 6**a,b). In contrast, $GA_{9.25}$ exhibited relatively uniform and compact Li growth without dendrite formation (Figure 6c,d). The $GA_{9.25}$ layers were almost embedded in the Li deposits, which makes them difficult to observe except for partial areas, as indicated by the arrow (Figure 6c). $GA_{9.25}$ demonstrated dendrite-free growth in the Li depositions, benefiting from both the GO and AgNW layers and their interdigitated nanostructure.

2.3. Electrochemical Performance of GO/AgNW LbL Thin-Films for Li-Plating and Stripping

The Li plating and stripping behavior of Cu, $G_{9.5}$, $A_{9.5}$, and $GA_{9.25}$ were examined in half-cell tests with Li/Cu or Li/LbL-coated-Cu using 1M LiTFSI in DOL/DME (1:1) electrolytes, without $LiNO_3$ additives, at a current density of 1 mA cm^{-2} and a capacity of 1 mAh cm^{-2} (**Figure 7**a). In order to remove surface contamination and stabilize the initial SEI formation, the Li/Cu and Li/LbL-coated-Cu half cells were pre-cycled five times from 0 to 1 V at a current density of 0.05 mA cm^{-2} before the cycling proceeded. Cu and $G_{9.5}$ exhibited low cycle stabilities with early drops of CEs from ≈20 cycles due to lithiophobicity and low electrical conductivity, respectively. $A_{9.5}$ and $GA_{9.25}$, which have high Li affinity, exhibit higher CE values and prolonged cycles compared to the two previous samples. However, the CE values of the $A_{9.5}$ sample decreased after 120 cycles, possibly due to pulverizations caused by repetitive alloying and dealloying during cycling.[49] The charge/discharge profiles showed relatively stable stripping behavior for $GA_{9.25}$ during the 1st and 30th cycles in comparison to the other samples (Figure S7, Supporting Information).

CV of the half cells was performed using 1 M LiTFSI in DOL/DME (1:1) with 1 wt% $LiNO_3$ additives at a scan rate of 0.1 mV s^{-1}. For $GA_{9.25}$ (Figure 7b), a Li–Ag alloy formation peak appeared near 0 V during the first Li plating, and dealloying peaks appeared below 0.5 V during stripping. Repetitive cycles for $GA_{9.25}$ demonstrated stable alloying and dealloying reactions, with no notable changes in the related peaks.[50,51] Conversely, the broad SEI formation peaks above 0.5 V disappeared after the first cycle, which indicates stable SEI formations during the first cycle (Figure 7b; Figure S8a, Supporting Information).[52,53] XPS analysis for the $GA_{9.25}$ suggests the SEI layer comprised a mixed interphase with Li—F and C—F components (Figure S9d, Supporting Information).[54] Each component of the LbL samples, $G_{9.5}$ and $A_{9.5}$, showed a dominant presence of Li—F and C—F phases, respectively (Figure S9a,b, Supporting Information).[55] Therefore, the presence of GO layers can be attributed to the more stable Li—F phases in $GA_{9.25}$. This is consistent with the CV results of $G_{9.5}$ (Figure S8c, Supporting Information), which showed the same SEI formation peaks as those in $G_{9.25}$. In contrast, $A_{9.5}$ featured only CV peaks from the alloying-dealloying reactions without a notable presence of SEI-formation peaks (Figure S8d, Supporting Information). Cu exhibited very weak SEI-formation peaks without alloy peaks (Figure S8b, Supporting Information). These results indicate that $GA_{9.25}$ benefits from the combined

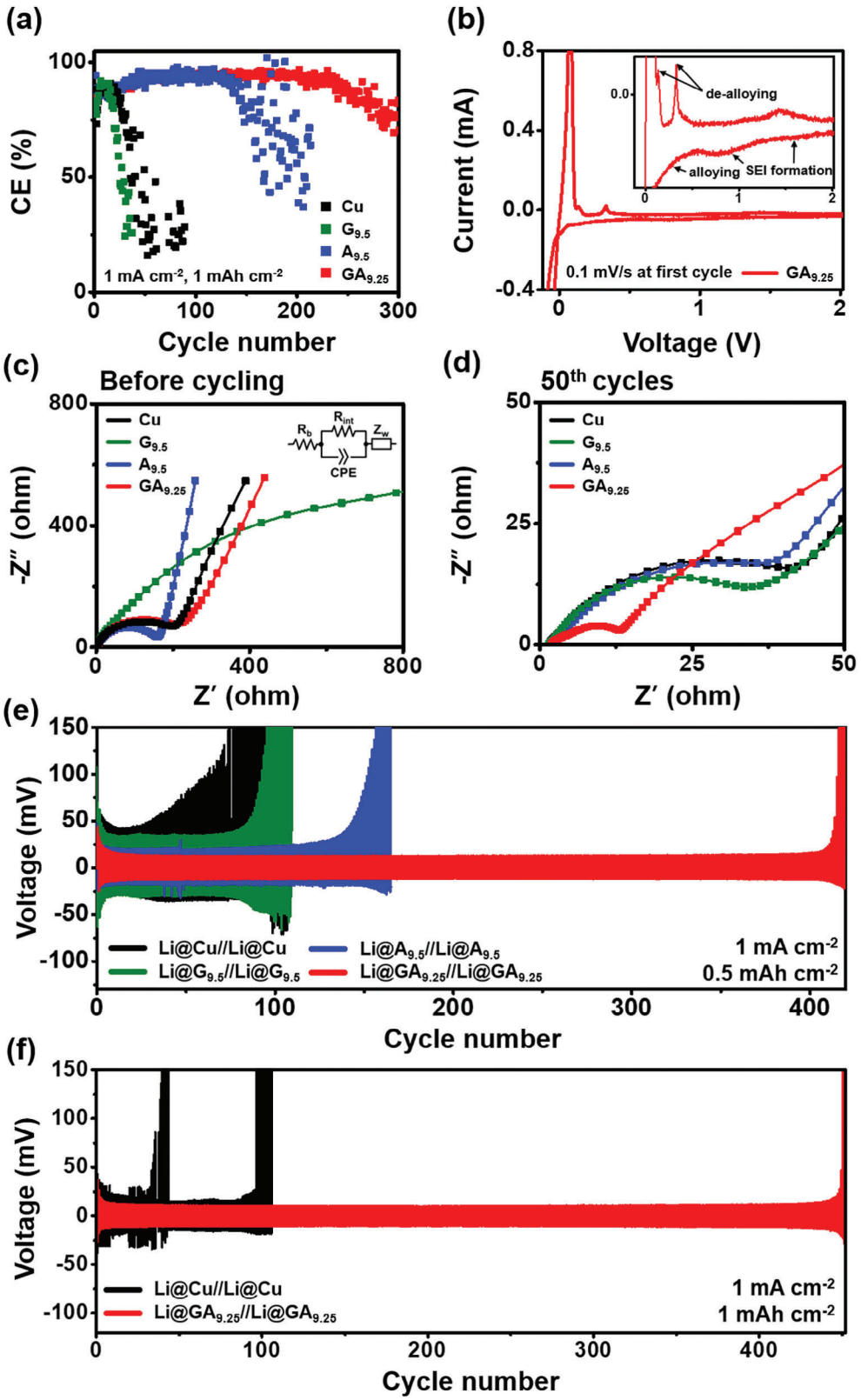

Figure 7. a) CE of Cu, $G_{9.5}$, $A_{9.5}$, and $GA_{9.25}$ at 1 mA cm^{-2}, 1 mAh cm^{-2} without $LiNO_3$ additive in DOL/DME (1:1) electrolyte. b) Cyclic voltammetry (CV) curves of half cells of $GA_{9.25}$ measured at a scan rate of 0.1 mV s^{-1} (inset: enlarged view of CV curves). Electrochemical impedance spectroscopy (EIS) of half cells of the samples c) before cycling and d) after 50 cycles (inset: equivalent circuit utilized for data analyses). Cycle-voltage profiles of symmetric cells with different capacities of Li pre-deposited on samples e) 2 mAh cm^{-2} (test at 1 mA cm^{-2}, 0.5 mAh cm^{-2}) and f) 4 mAh cm^{-2} (test at 1 mA cm^{-2}, 1 mAh cm^{-2}). Except for (a), all tests were conducted in 1 M LiTFSI in DOL/DME (1:1) electrolyte with 1 wt% $LiNO_3$ additives.

effects of both GO and AgNW, stable SEI formation, and reversible Li–Ag alloy reactions.

EIS was performed in half-cell configurations using an electrolyte of 1 M LiTFSI in DOL/DME (1:1) with 1 wt% $LiNO_3$ additives (Figure 7c,d; Figure S10, Supporting Information). The results were fitted using a simplified equivalent-circuit model (inset in Figure 7c; Figure S10, Supporting Information), where R_b, R_{int}, *CPE*, and Z_w represent bulk resistance, interfacial resistance, capacitance, and Warburg impedance, respectively (Table S4, Supporting Information). Before cycling, R_{int} for Cu, $A_{9.5}$, and $GA_{9.25}$ showed similar magnitudes of ≈200 Ω, except for $G_{9.5}$ (Figure 7c). This is possibly due to relatively thick insulating GO layers (Table S3, Supporting Information). Upon increasing the cycle numbers to 10 and 50 cycles, $GA_{9.25}$ showed the lowest R_{int} (≈10 Ω) among the samples (Figure 7d; Figure S10, Supporting Information). In comparison, other samples showed R_{int} of ≈35 Ω after 50 cycles. This indicates that the SEI layers in $GA_{9.25}$ are the least resistant to charge transfers and remain stable during cycling compared to the other tested samples.[56,57]

In addition, the rate capabilities of the Li/Cu and Li/LbL-coated-Cu half cells were further tested to investigate the resistance to Li-ion transport (Figure S11, Supporting Information). For pre-cycling, Li was plated at 0.5 mA cm^{-2}, with a capacity of 4 mAh cm^{-2}, and stripped at a cut-off voltage of 1 V to investigate the Li-ion transport behavior of the LbL samples.[18,58] The current densities were varied in the sequence 0.5-1-2-3-5-0.5 mA cm^{-2}. At each current density, a fixed amount of Li, with a capacity of 0.5 mAh cm^{-2}, was plated onto the Cu sides and stripped for 10 cycles, with the voltage cut off at 1 V. $G_{9.5}$ showed the lowest overpotentials at every current density, indicating least resistance to Li-ion transport among the LbL samples. Note that $A_{9.5}$ showed high overpotentials, presumably due to dendrite growth from excessive pre-cycling. In addition, the overpotentials of $G_{9.5}$ and $GA_{9.25}$ at the initial and final stages at 0.5 mA cm^{-2} were almost identical. The discharge capacity of $G_{9.5}$ and $GA_{9.25}$ was higher than the other two samples. These results confirm that GO layers contributed to fast Li-ion transport and stable SEI layer formation for $G_{9.5}$ and $GA_{9.25}$, which is also consistent with the previous EIS results. Additionally, the contact angles of Cu and $GA_{9.25}$ were measured by dropping liquid electrolytes onto the surfaces to investigate electrolyte wettability (Figure S12, Supporting Information). The electrolyte wettability of $GA_{9.25}$ was enhanced by the various functional groups of GO coated on the top layer, which reduced the contact angle by more than three times compared to Cu.[59]

The galvanostatic cycling performance of the Li symmetric cells was examined with respect to long-term cyclability (Figure 7e,f). Pre-deposition samples were utilized in the following symmetric and full-cell tests to avoid the deteriorating effects associated with the consumption of the initial Li deposition.[14] The same samples were used for both electrodes and tested with 1 M LiTFSI in DOL/DME (1:1) electrolyte with 1 wt% $LiNO_3$. First, the electrodes with pre-depositions of 2 mAh cm^{-2} were tested at 1 mA cm^{-2} and 0.5 mAh cm^{-2} (Figure 7e). The Li@Cu symmetric cell exhibited instability, with gradual overpotential increases, followed by a short circuit at ≈100 cycles. The Li@$G_{9.5}$ symmetric cell showed relatively stable voltage profiles, with an overpotential value of ≈35 mV, in comparison to the Li@Cu symmetric cells, but shorted at a similar cycle count. The Li@$A_{9.5}$ symmetric cell demonstrated relatively low overpotentials of ≈20 mV, with cycle longevity extending up to 135 cycles before a sharp increase in overpotential. In contrast, the Li@$GA_{9.25}$ symmetric cell demonstrated stable cycling for ≈400 cycles with an overpotential of ≈10 mV. In particular, the Li@$GA_{9.25}$ symmetric cell exhibited a stable long-term cycle by maintaining an overpotential of ≈10 mV in a square shape in all early, middle, and late cycle sections (Figure S13a, Supporting Information). Other samples exhibited higher overpotentials with more significant fluctuations (Figure S13b, Supporting Information). Li@Cu and Li@$GA_{9.25}$ symmetric cells with higher Li-pre-depositions of 4 mAh cm^{-2} were further tested at 1 mA cm^{-2} and 1 mAh cm^{-2} (Figure 7f). The Li@Cu symmetric cell exhibited unstable cycling performance from the beginning of the cycle. In contrast, the Li@$GA_{9.25}$ symmetric cell maintained a stable square-shaped overpotential profile for up to 450 cycles with a low overpotential of ≈10 mV for all cycles (Figure S14, Supporting Information). The Li@$GA_{9.25}$ symmetric cell exhibited excellent cycling stability during the Li-plating/stripping process.

2.4. Battery Performance of the LFP/Li@GA Full Cells

The Li@$GA_{9.25}$, with pre-deposition of 2 mAh cm^{-2} and 4 mAh cm^{-2}, were tested with LFP cathodes having a mass-loading of 6–7 mg cm^{-2} for full cell tests. All full cells were tested with 1 M LiTFSI in DOL/DME (1:1) with 1 wt% $LiNO_3$. The control sample of LFP/Li@Cu full cells was also tested, excluding $A_{9.5}$ and $G_{9.5}$ due to their low stabilities. LFP/Li@Cu and LFP/Li@$GA_{9.25}$ full cells were subjected to step cycle tests at various current densities (0.1-0.5-1-2-5-0.1 C) (**Figure 8a**; Figure S15a, Supporting Information). The LFP/Li@Cu and LFP/Li@$GA_{9.25}$ full cells, with a pre-deposition of 2 mAh cm^{-2}, exhibited increased capacity differences as the C-rate increased (Figure 8a). At 5 C, the specific capacity of the LFP/Li@$GA_{9.25}$ full cell was 89.2 mAh g^{-1}, with a capacity retention rate of ≈58.2%, which is 18.9% greater than the 75.0 mAh g^{-1} observed for the LFP/Li@Cu full cell. In addition, the charge-discharge curves of the LFP/Li@$GA_{9.25}$ full cell showed slight increases in polarization voltages as current densities increased (Figure 8b; Figure S15b, Supporting Information). The full cells with higher Li pre-depositions of 4 mAh cm^{-2} exhibited a similar trend in the step cycle tests but with smaller gaps in capacity differences compared to the tests with Li pre-depositions of 2 mAh cm^{-2} (Figure S15a, Supporting Information).

Long-term cycling tests of full cells with Li pre-depositions of 4 mAh cm^{-2} (N/P ratio = 3.36) were performed at 1 C (Figure 8c). The number of stable cycles was counted when the capacity retention fell below 80%. LFP/Li@$GA_{9.25}$ full cells operated stably up to 430 cycles with an average CE of 99.7%. In contrast, the LFP/Li@Cu full cells showed a significant decrease in discharge capacity at ≈220 cycles, which is accompanied by the onset of large fluctuations in CE. Furthermore, the full cells assembled from different $GA_{n.25}$ samples with n = 1, 5, and 15 were tested for comparison (Figure S16, Supporting Information). As the number of quadruple layers increased from 1 to 9, cycle longevities increased to 270, 322, and 430 cycles. However, for n = 15 with excessive deposition, the LFP/Li@$GA_{15.25}$ full cell showed reduced cycle stability, which is possibly due to increased resistance associated with the thicker GA layers (Table S5,

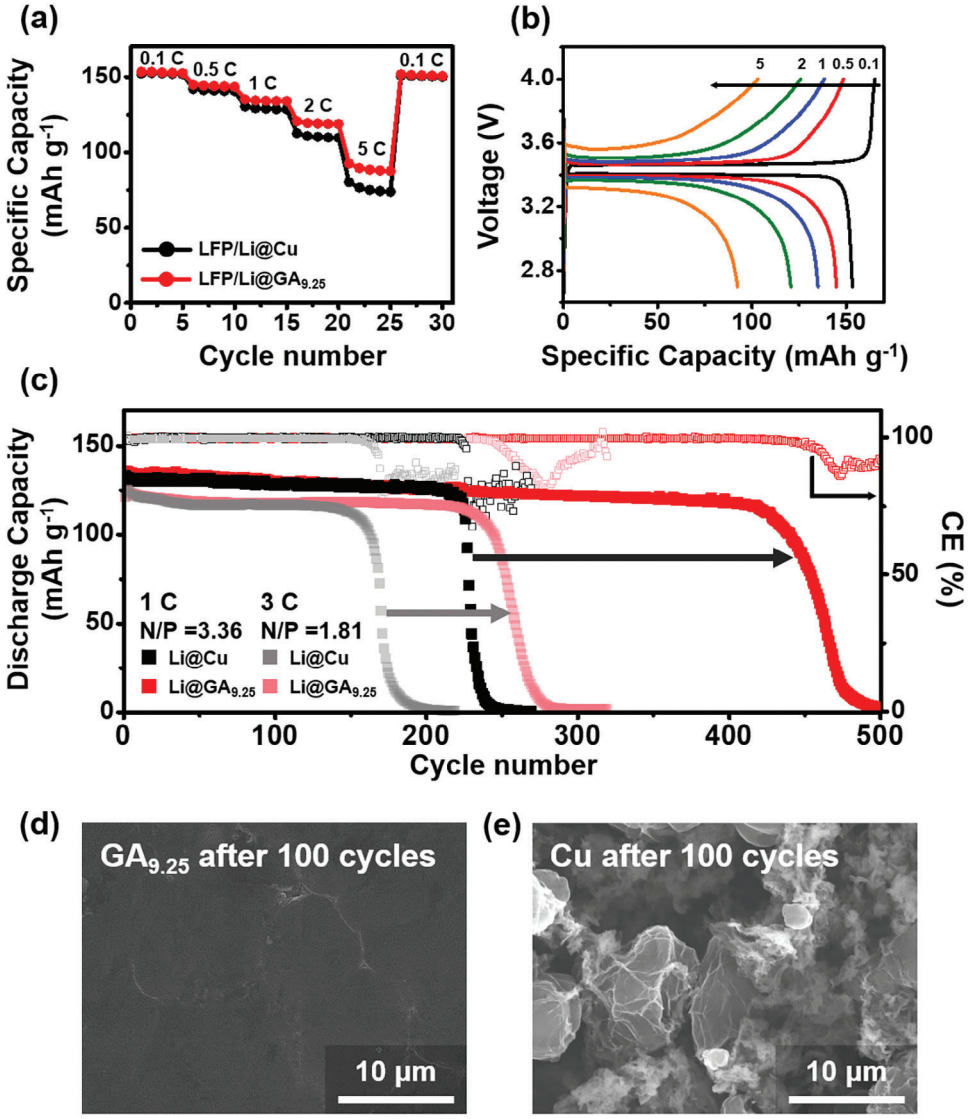

Figure 8. a) Rate performances of a full cell after Li plating with 2 mAh cm^{-2} at different current rates, ranging from 0.1 to 5 C, compared to LFP/Li@Cu and LFP/Li@$GA_{9.25}$. b) Charge/discharge curves of LFP/Li@$GA_{9.25}$ full cell at various current rates. c) Cycle performance and Coulombic efficiency of LFP/Li@Cu and LFP/Li@$GA_{9.25}$ full cells after Li plating with capacities of 4 mAh cm^{-2} at 1 C and 2 mAh cm^{-2} at 3 C. FE-SEM images of the anode surfaces from the disassembly of d) LFP/Li@$GA_{9.25}$ and e) LFP/Li@Cu full cells after 100 cycles at 1 C. The pre-deposition of Li in the samples was 4 mAh cm^{-2}.

Supporting Information).[60,61] LFP/Li@$GA_{9.25}$ full cells were also tested under high C-rate conditions of 3 C (Figure S15c, Supporting Information). These cells maintained 80% capacity up to 240 cycles, whereas LFP/Li@Cu full cells exhibited unstable capacity retention, with degradation starting ≈50 cycles and rapid failure before reaching 200 cycles. In addition, the LFP/Li@$GA_{9.25}$ full cells demonstrated the lowest irreversible capacities during the first charging cycles, which were attributed to the SEI formation, among the tested samples at both 1 C (Figure S17a,b, Supporting Information) and 3 C (Figure S17c, Supporting Information) rates.[62,63]

Li@$GA_{9.25}$ and Li@Cu full cells with Li pre-depositions of 2 mAh cm^{-2} (N/P ratio = 1.81) were also tested at 1 and 3 C-rates (Figure S18, Supporting Information; Figure 8c). The Li@$GA_{9.25}$ full cells could run up to 255 and 250 cycles for 1 C and 3 C-rates, respectively, before capacity retention fell below 80%. Both results were extended by ≈50 and 100 cycles compared to the Li@Cu full cells. For the very low N/P ratio of 1.18, with a high cathode-mass-loading of LFP (10 mg cm^{-2}), cycle stability was improved to 125 cycles compared to 95 cycles for the Li@Cu full cells (Figure S19, Supporting Information). The FE-SEM image of the anode surface from LFP/Li@$GA_{9.25}$ full cells after 100 cycles at 1 C showed a surprisingly flat and compact morphology (Figure 8d). This is in stark contrast to the image from the Cu anode surface disassembled from LFP/Li@Cu full cells after 100 cycles, which displayed dendritic Li deposits with accumulations of dead Li (Figure 8e). A summary of recent papers on lithiophilic current collector modification for Li-metal anodes is given

in Table S1 (Supporting Information). Particularly at the low N/P ratio of 1.81, the $GA_{9.25}$ full cells demonstrated remarkable performance, with a lifespan of 255 cycles at a rate of 1 C. Even at a high 3 C-rate, which was rarely tested in other studies, it showed remarkable performance and achieved a lifespan of 250 cycles at the same N/P ratio of 1.81.

3. Conclusion

We successfully fabricated GO and AgNW thin films on Cu foils with a highly interdigitated nanostructure using an LbL assembly method. Homogeneous and stable film deposition was achieved by incorporating a bi-functional cross-linker (MEA) between each layer to promote specific bonding interaction. The GO layers facilitated the distribution of Li ionic flux, which led to smoother Li deposits and stable SEI layer formation. The AgNW layers acted as nucleation sites for the initial Li deposition and enabled Li–Ag alloy and lowering of the nucleation overpotentials. $GA_{9.25}$ exhibited a dense morphology for Li deposits without dendrite formations at different Li-deposition capacities (from 0.2 to 4 mAh cm^{-2}) due to the benefits of both GO and AgNW layers and their interdigitated nanostructure. As a result, the $Li@GA_{9.25}$ symmetric cell tests reveal stable Li-plating and stripping for 400 cycles. The $LFP/Li@GA_{9.25}$ full cell, pre-deposited with Li at 4 mAh cm^{-2}, demonstrated high stability (430 cycles) with an average CE of 99.7% at 1 C. Even with a low N/P ratio of 1.81, which reduced the Li pre-deposited capacity by half, the cell achieved 255 cycles with an average CE of 99.5%. In addition, it demonstrated excellent cycling performance, reaching 250 cycles even at a high charge/discharge rate of 3 C. The flat morphology of the Li deposit after 100 cycles confirms the benefits of the $GA_{9.25}$ film coating on Cu foils. Therefore, the $GA_{9.25}$ film, which was prepared using LbL methods, offers a simple and effective approach for fabricating highly interdigitated thin film electrodes for high-energy Li-metal batteries.

Supporting Information

Supporting Information is available from the Wiley Online Library or from the author.

Acknowledgements

The authors gratefully acknowledge the financial support from the National Research Foundation of Korea (NRF) grant funded by the Korean Government (Ministry of Science and ICT) (nos. RS-2024-00408951, RS-2024-00453713, and RS-2024-00335171), Technology Development Program (RS-2023-00269781) funded by the Ministry of SMEs and Startups (MSS, Korea), and Korea Basic Science Institute (National Research Facilities and Equipment Center) funded by the Ministry of Education (RS-2024-00436346).

Conflict of Interest

The authors declare no conflict of interest.

Data Availability Statement

The data that support the findings of this study are available from the corresponding author upon reasonable request.

Keywords

graphene oxide, layer-by-layer assembly, Li dendrite suppression, Li-metal anodes, silver nanowire

Received: December 30, 2024
Published online:

[1] X. B. Cheng, R. Zhang, C. Z. Zhao, Q. Zhang, *Chem. Rev.* **2017**, *117*, 10403.
[2] D. Lin, Y. Liu, Y. Cui, *Nat. Nanotechnol.* **2017**, *12*, 194.
[3] Z. Li, J. Huang, B. Y Liaw, V. Metzler, J. Zhang, *J. Power Sources* **2014**, *254*, 168.
[4] S. S. Zhang, *ACS Appl. Energy Mater.* **2018**, *1*, 910.
[5] K. Cai, G. Zhong, H. Zheng, G. Kang, R. Yin, T. Jia, S. Huang, K. Yu, L. Peng, F. Kang, Y. Cao, *ACS Appl. Mater. Interfaces* **2022**, *14*, 45433.
[6] C. Niu, H. Lee, S. Chen, Q. Li, J. Du, W. Xu, J. G. Zhang, M. S. Whittingham, J. Xiao, J. Liu, *Nat. Energy* **2019**, *4*, 551.
[7] Y. Liu, D. Gao, H. Xiang, X. Feng, Y. Yu, *Energy Fuels* **2021**, *35*, 12921.
[8] K. Yan, Z. Lu, H. W. Lee, F. Xiong, P. C. Hsu, Y. Li, J. Zhao, S. Chu, Y. Cui, *Nat. Energy* **2016**, *1*, 16010.
[9] A. Pei, G. Zheng, F. Shi, Y. Li, Y. Cui, *Nano Lett.* **2017**, *17*, 1132.
[10] J. Liu, Z. Bao, Y. Cui, E. J. Dufek, J. B. Goodenough, P. Khalifah, Q. Li, B. Y. Liaw, P. Liu, A. Manthiram, Y. S. Meng, V. R. Subramanian, M. F. Toney, V. V. Viswanathan, M. S. Whittingham, J. Xiao, W. Xu, J. Yang, X. Q. Yang, J. G. Zhang, *Nat. Energy* **2019**, *4*, 180.
[11] Q. Wang, B. Liu, Y. Shen, J. Wu, Z. Zhao, C. Zhong, W. Hu, *Adv. Sci.* **2021**, *8*, 2101111.
[12] X. Li, R. Zhu, H. Jiang, Y. Yu, W. Wan, X. Li, C. Wang, Y. Huang, *J. Mater. Chem. A* **2022**, *10*, 11246.
[13] G. Zheng, S. W. Lee, Z. Liang, H. W. Lee, K. Yan, H. Yao, H. Wang, W. Li, S. Chu, Y. Cui, *Nat. Nanotechnol.* **2014**, *9*, 618.
[14] S. Cui, P. Zhai, W. Yang, Y. Wei, J. Xiao, L. Deng, Y. Gong, *Small* **2020**, *16*, 1905620.
[15] N. H. Hawari, X. Huang, L. M. Butarbutar, A. Prayogi, H. N. Hidayat, A. Sumboja, N. Ding, *J. Alloys Compd.* **2024**, *975*, 172988.
[16] N. Zhang, S. H. Yu, H. D. Abruña, *Nano Res.* **2020**, *13*, 45.
[17] J. Ma, J. Yang, C. Wu, M. Huang, J. Zhu, W. Zeng, L. Li, P. Li, X. Zhao, F. Qiao, Z. Zhang, D. He, S. Mu, *Energy Storage Mater.* **2023**, *56*, 572.
[18] T. Foroozan, F. A. Soto, V. Yurkiv, S. Sharifi-Asl, R. Deivanayagam, Z. Huang, R. Rojaee, F. Mashayek, P. B. Balbuena, R. Shahbazian-Yassar, *Adv. Funct. Mater.* **2018**, *28*, 1705917.
[19] V. Jabbari, V. Yurkiv, A. Ghorbani, F. Mashayek, R. Shahbazian-Yassar, *Energy Adv.* **2023**, *2*, 712.
[20] Z. T. Wondimkun, T. T. Beyene, M. A. Weret, N. A. Sahalie, C. J. Huang, B. Thirumalraj, B. A. Jote, D. Wang, W. N. Su, C. H. Wang, G. Brunklaus, M. Winter, B. J. Hwang, *J. Power Sources* **2020**, *450*, 227589.
[21] L. Luo, S. Xia, X. Zhang, J. Yang, S. Zheng, *Adv. Sci.* **2022**, *9*, 2104391.
[22] S. Jin, Y. Ye, Y. Niu, Y. Xu, H. Jin, J. Wang, Z. Sun, A. Cao, X. Wu, Y. Luo, H. Ji, L. J. Wan, *J. Am. Chem. Soc.* **2020**, *142*, 8818.
[23] M. Fan, B. Chen, K. Wang, Q. Yu, Y. Ding, Z. Lei, F. Liu, Y. Shen, G. He, *Mater. Today Energy* **2021**, *21*, 100751.
[24] Y. Jiang, W. Zhang, Y. Qi, Y. Wang, T. Hu, P. Li, C. Tian, W. Sun, Y. Liu, *Nanomaterials* **2023**, *13*, 1400.
[25] D. Rehnlund, F. Lindgren, S. Böhme, T. Nordh, Y. Zou, J. Pettersson, U. Bexell, M. Boman, K. Edström, L. Nyholm, *Energy Environ. Sci.* **2017**, *10*, 1350.
[26] S. Li, Y. Ma, J. Ren, H. Liu, K. Zhang, Y. Zhang, X. Tang, W. Wu, C. Sun, B. Wei, *ACS Appl. Energy Mater.* **2019**, *2*, 3642.

[27] P. Xue, S. Liu, X. Shi, C. Sun, C. Lai, Y. Zhou, D. Sui, Y. Chen, J. Liang, *Adv. Mater.* **2018**, *30*, 1804165.
[28] K. Ariga, J. P. Hill, Q. Ji, *Phys. Chem. Chem. Phys.* **2007**, *9*, 2319.
[29] C. Wang, M. J. Park, H. Yu, H. Matsuyama, E. Drioli, H. K. Shon, *J. Membr. Sci.* **2022**, *661*, 120926.
[30] Y. Ko, S. Lee, C. H. Kwon, S. W. Lee, J. Cho, *Adv. Energy Mater.* **2021**, *11*, 2002969.
[31] S. Lee, Y. Song, Y. Ko, Y. Ko, J. Ko, C. H. Kwon, J. Huh, S. W. Kim, B. Yeom, J. Cho, *Adv. Mater.* **2020**, *32*, 1906460.
[32] S. Lee, Y. Song, J. Cho, Y. J. Jang, B. Yeom, *ACS Appl. Energy Mater.* **2023**, *6*, 10961.
[33] J. J. Richardson, J. Cui, M. Björnmalm, J. A. Braunger, H. Ejima, F. Caruso, *Chem. Rev.* **2016**, *116*, 14828.
[34] X. Zhang, Y. Xu, X. Zhang, H. Wu, J. Shen, R. Chen, Y. Xiong, J. Li, S. Guo, *Prog. Polym. Sci.* **2019**, *89*, 76.
[35] A. J. Mateos, A. A. Cain, J. C. Grunlan, *Ind. Eng. Chem. Res.* **2014**, *53*, 6409.
[36] X. Zhang, J. Wang, H. Jia, B. Yin, L. Ding, Z. Xu, Q. Ji, *RSC Adv.* **2016**, *6*, 54668.
[37] M. K. Rabchinskii, V. V. Shnitov, A. T. Dideikin, A. E. Aleksenskii, S. P. Vul, M. V. Baidakova, I. I. Pronin, D. A. Kirilenko, P. N. Brunkov, J. Weise, S. L. Molodtsov, *J. Phys. Chem. C* **2016**, *120*, 28261.
[38] S. Saxena, T. A. Tyson, S. Shukla, E. Negusse, H. Chen, J. Bai, *Appl. Phys. Lett.* **2011**, *99*, 12274.
[39] Y. Sun, B. Gates, B. Mayers, Y. Xia, *Nano Lett.* **2002**, *2*, 165.
[40] Z. Wang, J. Liu, X. Chen, J. Wan, Y. Qian, *Chem. – A Eur. J.* **2005**, *11*, 160.
[41] X. L. Li, S. Huang, D. Yan, J. Zhang, D. Fang, Y. Von Lim, Y. Wang, T. C. Li, Y. Li, L. Guo, H. Y. Yang, *Energy Environ. Mater.* **2023**, *6*, 12274.
[42] S. D. Techane, L. J. Gamble, D. G. Castner, *Biointerphases* **2011**, *6*, 98.
[43] G. Jalani, M. Cerruti, *Nanoscale* **2015**, *7*, 9990.
[44] S. Park, K. S. Lee, G. Bozoklu, W. Cai, S. B. T. Nguyen, R. S. Ruoff, *ACS Nano* **2008**, *2*, 572.
[45] D. Knorr, N. Tran, K. Williams, J. Andzelm, N. Henry, K. Gaskell, J. Lenhart, N. Baril, C. Jaye, D. Fischer, M. Tidrow, S. Bandara, *Appl. Surf. Sci.* **2018**, *462*, 489.
[46] A. Liu, Y. Li, D. Shu, Y. Zhou, *Fullerenes Nanotub. Carbon Nanostructures* **2021**, *29*, 407.
[47] L. Ye, C. Zhang, Y. Zhou, B. Ülgüt, Y. Zhao, J. Qian, *J. Energy Chem.* **2022**, *74*, 412.
[48] O. C. Compton, S. T. Nguyen, *Small* **2010**, *6*, 711.
[49] B. Du, C. Shen, T. Wang, C. Sun, *Electrochim. Acta* **2023**, *439*, 141690.
[50] Y. Jiang, Q. Lv, C. Bao, B. Wang, P. Ren, H. Zhong, Y. Yang, X. Liu, Y. Dong, F. Jin, D. Wang, T. Xiong, H. Liu, S. Dou, J. Wang, J. Xue, *Cell Rep. Phys. Sci.* **2022**, *3*, 100785.
[51] Y. Hu, Y. Chen, X. Wang, P. Zhou, L. He, L. Chen, M. Zhang, *Nano Lett.* **2024**, *24*, 9178.
[52] J. Zhang, Z. Xie, W. Li, S. Dong, M. Qu, *Carbon* **2014**, *74*, 153.
[53] J. H. Lee, W. H. Shin, S. Y. Lim, B. G. Kim, J. W. Choi, *Mater. Renew. Sustain. Energy* **2014**, *3*, 22.
[54] M. He, R. Guo, G. M. Hobold, H. Gao, B. M. Gallant, *Proc. Natl. Acad. Sci. USA* **2020**, *117*, 73.
[55] T. Wang, G. Xie, J. Zhu, B. Lu, *Electrochim. Acta* **2015**, *186*, 64.
[56] S. Ni, M. Zhang, C. Li, R. Gao, J. Sheng, X. Wu, G. Zhou, *Adv. Mater.* **2023**, *35*, 2209028.
[57] Z. Peng, F. Ren, S. Yang, M. Wang, J. Sun, D. Wang, W. Xu, J. G. Zhang, *Nano Energy* **2019**, *59*, 110.
[58] H. Tian, Z. W. Seh, K. Yan, Z. Fu, P. Tang, Y. Lu, R. Zhang, D. Legut, Y. Cui, Q. Zhang, *Adv. Energy Mater.* **2017**, *7*, 1602528.
[59] Z. T. Wondimkun, W. A. Tegegne, J. Shi-Kai, C. J. Huang, N. A. Sahalie, M. A. Weret, J. Y. Hsu, P. L. Hsieh, Y. S. Huang, S. H. Wu, W. N. Su, B. J. Hwang, *Energy Storage Mater.* **2021**, *35*, 334.
[60] R. Zhao, J. Liu, J. Gu, *Appl. Energy* **2015**, *139*, 220.
[61] Y. Zhang, L. Miao, J. Ning, Z. Xiao, L. Hao, B. Wang, L. Zhi, *2D Mater.* **2015**, *2*, 024013.
[62] J. S. Edge, S. O'Kane, R. Prosser, N. D. Kirkaldy, A. N. Patel, A. Hales, A. Ghosh, W. Ai, J. Chen, J. Yang, S. Li, M. C. Pang, L. Bravo Diaz, A. Tomaszewska, M. W. Marzook, K. N. Radhakrishnan, H. Wang, Y. Patel, B. Wu, G. J. Offer, *Phys. Chem. Chem. Phys.* **2021**, *23*, 8200.
[63] Y. Cheng, J. Chen, Y. Chen, X. Ke, J. Li, Y. Yang, Z. Shi, *Energy Storage Mater.* **2021**, *38*, 276.